scientific reports

Check for updates

OPEN

Hydroxyl groups tune the pH sensitivity of Imidazo[4,5-*b*] pyridine acrylonitrile derivatives as revealed by spectroscopy and DFT calculations

Ida Boček Pavlinac[1], Mirna Dragić[1], Marina Galić[1], Ana Čikoš[2], Marijana Hranjec[1]✉ & Robert Vianello[3]✉

We investigated the potential of imidazo[4,5-*b*]pyridine acrylonitrile derivatives as pH sensors, focusing on their spectroscopic responses to varying pH conditions. By incorporating different numbers of hydroxyl groups and evaluating the role of the unsubstituted NH group on the heterocyclic core, we characterized their UV–Vis absorption properties in solvents of variable polarity and buffer solutions (pH 1–13). The results demonstrate significant solvatochromic behavior, with hydroxyl group substitution and NH proton availability driving bathochromic and hypsochromic shifts. UV–Vis pH titrations revealed enhanced sensitivity in compounds with multiple hydroxyl groups, particularly in acidic and basic conditions. Computational DFT analysis identified the pyridine nitrogen as the primary protonation site and confirmed the role of phenolic hydroxyl groups in increasing acidity. NMR analysis validated these findings, showing chemical shift changes consistent with pyridine nitrogen protonation. Importantly, the combined experimental-computational approach enabled deconvolution of overlapping protonation equilibria and assignment of individual spectral features to specific protonation states. These compounds show promise as versatile pH sensors for optical sensing, optoelectronic purposes, and organo-electronic materials due to their robust spectroscopic properties. Notably, compound 8 emerged as an encouraging candidate for monitoring transitions from neutral to higher pH values, owing to its significant red shift in UV–Vis spectra near neutral pH, making it particularly suitable for detecting subtle alkalinity changes in environmental and biomedical applications.

Keywords Acrylonitrile derivatives, Density functional calculations, Imidazo[4,5-*b*]pyridines, NMR spectroscopy, Optical pH sensors, pK_a values, Solvatochromism

The reactivity of organic molecules toward pH changes depends strongly on the presence and positioning of functional groups capable of proton exchange[1]. Such moieties, typically nitrogen- or oxygen-based, play crucial roles in protonation–deprotonation equilibria that underlie pH-responsive behavior[2,3]. Among them, nitrogen heterocycles are particularly attractive scaffolds for designing optical pH sensors. They not only provide basic sites for protonation but also extend π-conjugation through their aromatic systems, thereby shifting absorption and emission into the visible region. Linking these heterocyclic cores to aromatic frameworks via conjugated linkers such as acrylonitriles further enhances their optical and electronic properties, enabling applications in sensing, optoelectronics, and photonics[4,5].

Acrylonitrile derivatives incorporating nitrogen heterocycles, including benzimidazole and imidazole systems, have been intensively explored due to their chemical robustness, rich photophysical behavior[6–8] and biological activity[9,10]. Many of these derivatives exhibit solvatochromism, aggregation-induced emission

[1]Department of Organic Chemistry, Faculty of Chemical Engineering and Technology, University of Zagreb, 10000 Zagreb, Croatia. [2]NMR Centre, Ruđer Bošković Institute, 10000 Zagreb, Croatia. [3]Laboratory for the Computational Design and Synthesis of Functional Materials, Division of Organic Chemistry and Biochemistry, Ruđer Bošković Institute, 10000 Zagreb, Croatia. ✉email: mhranjec@fkit.unizg.hr; robert.vianello@irb.hr

(AIE), and selective ion sensing[11,12], making them suitable for practical detection of anions such as CN^-[13] or nitroaromatics like picric acid[14]. For instance, benzimidazole-based acrylonitriles have shown colorimetric and fluorescence responses through hydrogen-bonding interactions involving the unsubstituted imidazole or benzimidazole NH group[15]. These findings highlight the central role of the NH proton in mediating the molecular response to external stimuli. Moreover, acrylonitrile derivatives conjugated with chromophoric units such as anthraquinone or diphenylimidazole have been successfully employed in reversible pH sensing and as emissive layers in OLEDs, illustrating the multifunctional nature of these materials.

Despite these advances, systematic investigations of imidazo[4,5-*b*]pyridine-based acrylonitriles remain scarce, particularly regarding how hydroxyl substitution and N–H functionality affect their acid–base and spectroscopic properties. The imidazo[4,5-*b*]pyridine scaffold offers a unique electronic structure combining two nitrogen atoms of different basicities, one pyridinic and one imidazolic, providing distinct protonation sites and thus tunable pH sensitivity. Moreover, introducing hydroxyl groups on the phenyl ring can modulate electron density through resonance and hydrogen bonding, potentially altering both acidity and solvatochromic behavior. However, the interplay of these effects has not yet been systematically explored. Despite the growing body of work on acrylonitrile-based chromophores and imidazo[4,5-*b*]pyridine derivatives, a systematic investigation of how hydroxyl substitution modulates coupled protonation equilibria and the resulting spectroscopic response in these hybrid systems remains lacking. In particular, systems featuring multiple proton-responsive sites often exhibit overlapping acid–base transitions, which complicates the assignment of individual spectral features and limits mechanistic interpretation. Addressing this challenge requires a combined experimental and computational approach capable of disentangling contributions from different protonation states.

In our previous work, imidazo[4,5-*b*]pyridine acrylonitrile derivatives have been investigated for their biological activity, showing significant antiproliferative effects by targeting tubulins[16–18] Building on these findings, we now extend our research toward understanding their optical and pH-sensing properties. Here, we present a comprehensive experimental and computational study of a series of imidazo[4,5-*b*]pyridine acrylonitrile derivatives (**7**–**11**) designed to tune pH sensitivity through controlled hydroxyl substitution and N–H functionality. By combining UV–Vis spectroscopy, NMR titrations, and DFT calculations, we elucidate how structural variations influence protonation and deprotonation equilibria, spectral shifts, and overall acidity. This integrated approach enables us to correlate experimental observations with theoretical predictions, thereby providing a deeper understanding of how subtle electronic modifications govern pH responsiveness.

Our results reveal that the number and position of hydroxyl groups significantly enhance pH sensitivity, while the presence of a free N–H proton on the imidazo[4,5-*b*]pyridine core is crucial for maintaining strong spectroscopic response. Notably, the monohydroxy-substituted derivative **8** shows a pronounced bathochromic shift near neutral pH, making it an excellent candidate for detecting slight alkalinity changes in environmental and biomedical applications. Beyond establishing these structure–property relationships, this work demonstrates the potential of hydroxyl-modified imidazo[4,5-*b*]pyridines as versatile chromophores for optical sensing, optoelectronic devices, and organo-electronic materials. Because several compounds in this series undergo multiple sequential protonation and deprotonation events with pK_a values separated by only 1–2 units, the resulting experimental UV–Vis titration curves contain overlapping absorptions. Therefore, TD-DFT calculations were employed to support the assignment of individual spectral components to specific protonation states.

Beyond conventional spectroscopic characterization, the present work aims to establish quantitative structure–property relationships and general design principles for tuning pH sensitivity in push–pull chromophores. By integrating UV–Vis titrations with TD-DFT calculations, we provide a molecular-level interpretation of overlapping spectral features, enabling assignment of individual absorption bands to distinct protonation forms. This approach offers a more detailed mechanistic understanding than typically achieved in similar systems and provides a predictive framework for the rational design of pH-responsive materials.

Results and discussion

Chemistry

Synthesis of potential pH sensing imidazo[4,5-*b*]pyridines is described in detail in our previous work along with the evaluation of their biological activity.[19] Compounds **7**–**11** bearing various number of hydroxyl groups were obtained in moderate to high yield by reacting 2-cyanomethyl derivatives of imidazo[4,5-*b*]pyridine **1** or **2** with corresponding benzaldehydes **3**–**6** (Scheme 1).

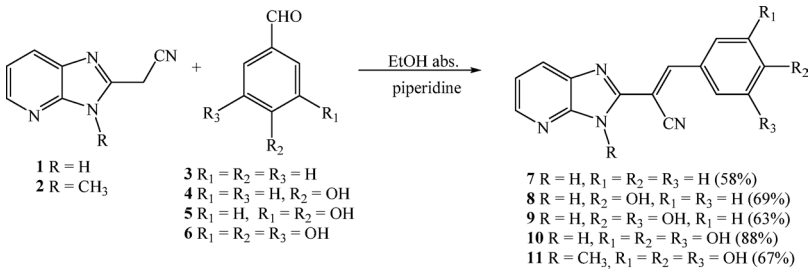

Scheme 1. Synthesis of hydroxy-substituted acrylonitriles of imidazo[4,5-*b*]pyridine.

Spectroscopic characterization

UV–Vis spectroscopy

In our investigation of the spectroscopic properties of studied imidazo[4,5-*b*]pyridine acrylonitrile derivatives, we explored how the number of hydroxyl groups and the presence of a free N–H proton on the heterocyclic core influence their spectral and pH-sensing properties. To this end, we synthesized N–H unsubstituted derivatives with zero to three hydroxyl groups (**7**–**10**) and an *N*3-methyl-substituted derivative (**11**) bearing three hydroxyl groups on the phenyl core. UV–Vis and emission spectra were recorded in organic solvents of varying polarity to ensure solubility and conduct preliminary spectroscopic studies (Table 1). Stock solutions were prepared in six solvents with diverse properties, including aromatic and aliphatic, polar and nonpolar, and protic and aprotic characteristics: acetonitrile, ethanol, ethyl acetate, methanol, Milli-Q water, and toluene. Absorption spectra of **7**–**11** were measured at a concentration of 2×10^{-5} mol dm^{-3} (Fig. 1), with dominant absorption bands attributed to π–π* electronic transitions, as confirmed by computational natural transition orbital analysis (Figures S1–S5). To facilitate a more direct comparison of spectral features among the studied systems, the absorption spectra in Fig. 1 are presented in normalized form (A/A_{max}). This representation emphasizes wavelength shifts and band shapes rather than absolute intensities, allowing clearer visualization of solvatochromic and substitution effects. The normalized spectra reveal that the gradual red shift from **7** to **10** corresponds to progressive extension of conjugation and enhanced intramolecular charge transfer with increasing hydroxyl substitution. In contrast, the spectrum of the *N*3-methylated derivative **11** remains blue-shifted and slightly narrower, confirming that the loss of the free N–H proton limits conjugation along the imidazo[4,5-*b*]pyridine core. These normalized comparisons thus highlight the structural origin of the observed solvatochromism and complement the quantitative data summarized in Table 1.

UV–Vis spectra revealed that the number of hydroxyl groups and *N*3-methyl substitution notably affect solvatochromism. For **7** with no –OH groups, absorption intensity strongly varied with solvent polarity, peaking in the most polar water and diminishing in the least polar toluene. Additionally, a bathochromic shift of ~ 6 nm was observed in toluene relative to water. The introduction of one hydroxyl group in **8** noticeably altered spectral responses, with the highest absorption intensities in water and toluene and the lowest in ethanol. Compared to water, small bathochromic shifts were observed in toluene (~ 5 nm), ethanol (~ 3 nm), and methanol (~ 2 nm), while hypsochromic shifts occurred in acetonitrile (~ 4 nm) and ethyl acetate (~ 2 nm). Increasing the number of hydroxyl groups in **9** and **10** led to even more pronounced changes in UV–Vis spectra, indicating a strong dependence on hydroxyl substitution.

Dihydroxy-substituted **9** and trihydroxy-substituted **10** exhibited the highest absorbance intensity in polar alcoholic solvents (methanol and ethanol) and the lowest in water. Relative to water, **9** showed bathochromic shifts in methanol (~ 8 nm) and ethanol (~ 11 nm), while less polar solvents (acetonitrile, ethyl acetate, and toluene) induced hypsochromic shifts of ~ 1–2 nm. The introduction of three hydroxyl groups in **10** resulted in larger bathochromic shifts in ethanol (~ 14 nm) and methanol (~ 11 nm) compared to water. *N*3-methyl substitution in **11** further altered the UV–Vis spectra, with the highest absorbance intensity in ethyl acetate and the lowest in water. Compared to water, **11** displayed bathochromic shifts in all tested solvents, with the largest shifts observed in ethanol (~ 21 nm), toluene (~ 16 nm), methanol (~ 14 nm), and ethyl acetate (~ 9 nm).

The data in Table 1 reveal clear correlations between molecular structure and spectroscopic response. As the number of hydroxyl substituents increases from **7** to **10**, absorption maxima become more sensitive to solvent polarity, reflecting enhanced intramolecular charge transfer (ICT) between the electron-donating phenolic units and the acrylonitrile acceptor. This manifests as gradual bathochromic shifts (up to ~ 45 nm) and higher ε values in polar solvents, consistent with stabilization of charge-separated excited states. In contrast, *N*3-methylation in **11** disrupts this conjugation pathway: by blocking the imidazole N–H donor, delocalization along the heterocyclic core is reduced, leading to overall hypsochromic shifts and diminished molar absorptivity. The experimentally

Compound	Solvent	Toluene	Ethyl acetate	Acetonitrile	Ethanol	Methanol	MQ water	
	E_T / 30	33.9	38.1	45.6	51.9	55.4	63.1	pK_a(exp)*
7	ε × 10^3 /dm^3 mol^{-1} cm^{-1}	18.6	19.4	19.4	19.4	19.4	19.5	2.4
	λ / nm	351	344	342	346	343	345	
8	ε × 10^3 /dm^3 mol^{-1} cm^{-1}	10.7	11.3	10.9	10.9	11.2	11.3	2.3 7.0
	λ / nm	372	365	363	370	369	367	
9	ε × 10^3 /dm^3 mol^{-1} cm^{-1}	78.5	84.5	81.9	86.0	83.5	75.5	2.3 6.7 10.6
	λ / nm	386	380	379	392	389	381	
10	ε × 10^3 /dm^3 mol^{-1} cm^{-1}	52.5	56.5	50.0	57.5	57.5	43.5	2.3 4.2 10.2
	λ / nm	396	384	382	399	396	385	
11	ε × 10^3 /dm^3 mol^{-1} cm^{-1}	34.5	37.0	33.0	34.0	33.5	32.0	2.3 6.0 11.3
	λ / nm	385	378	370	390	383	369	

Table 1. Spectroscopic data and measured pK_a values for characterized compounds. *pK_a values were determined in the aqueous solution.

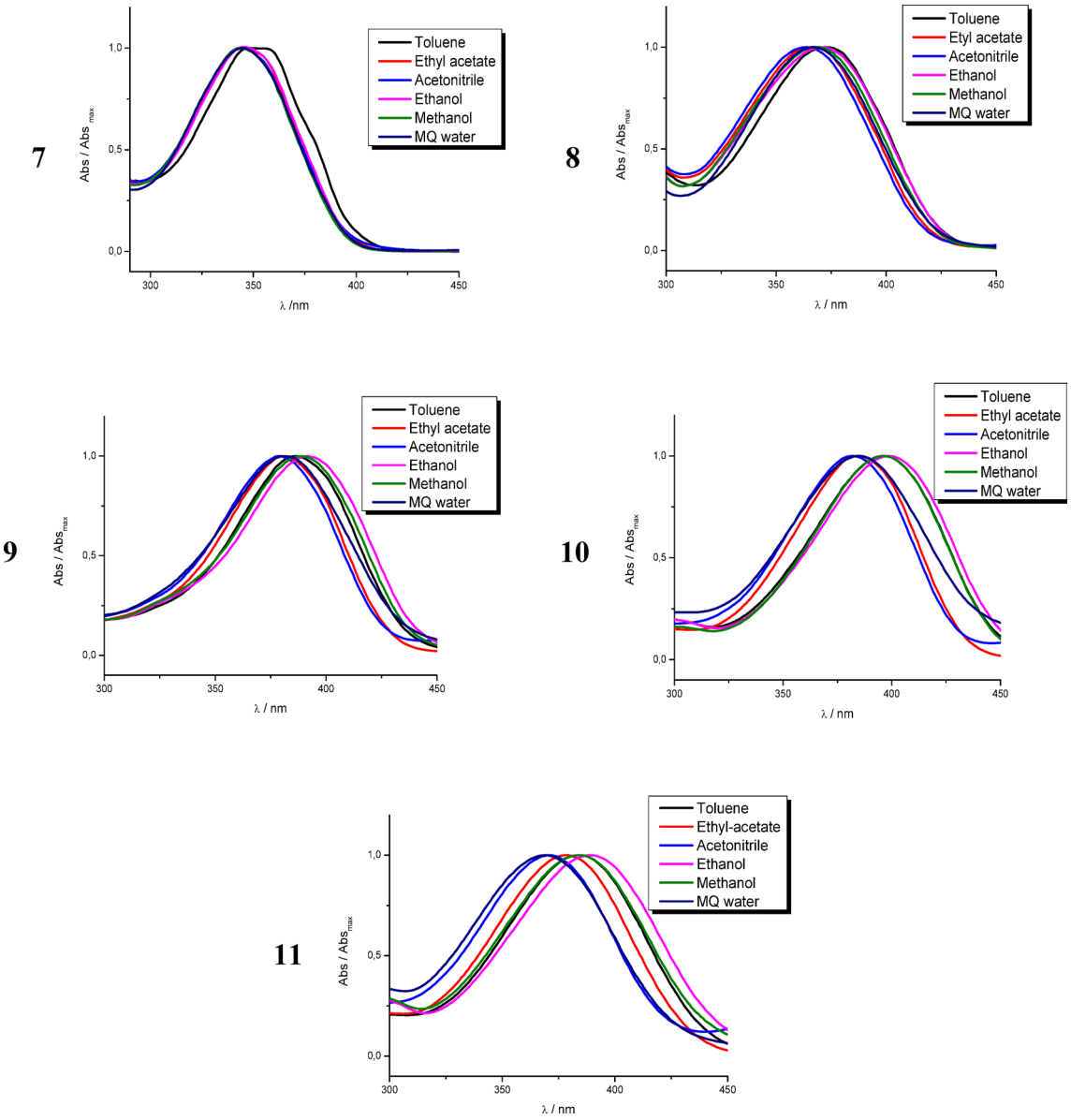

Fig. 1. Normalized UV–Vis absorption spectra (A/A_{max}) of **7**–**11** recorded at $c \approx 2 \times 10^{-5}$ mol dm^{-3} in solvents of varying polarity, emphasizing solvent-specific band evolution. Normalization enables direct comparison of spectral shapes and wavelength shifts among compounds. Compounds are shown in the order **7**, **8**, **9**, **10**, **11** to follow the progressive increase in hydroxyl substitution and the final *N*-methyl analogue.

determined pK_a values in aqueous solution further support these observations, as compounds bearing more hydroxyl groups show progressively lower pK_a values, owing to the cumulative electron-withdrawing influence and intramolecular hydrogen-bond stabilization of deprotonated phenolate forms. Collectively, these findings demonstrate that both hydroxyl substitution and N–H availability act cooperatively to fine-tune the photophysical and acid–base properties of imidazo[4,5-*b*]pyridine acrylonitriles, providing a molecular basis for their tunable pH sensitivity.

A notable feature in the UV–Vis spectra of **9**, **10**, and **11** in acetonitrile is the appearance of an additional absorption band at longer wavelengths (e.g., ~ 486 nm for **9**). This red-shifted band is absent in the other solvents examined and is not observed for the less substituted analogues **7** and **8**, indicating that its appearance depends on both molecular structure and solvent environment. The increased number of hydroxyl substituents enhances the electron-donating character of the aromatic ring, while the acrylonitrile moiety acts as an electron acceptor, favoring intramolecular electronic redistribution upon excitation. The polar aprotic nature and high dielectric constant of acetonitrile are expected to stabilize the corresponding excited state, thereby contributing to the appearance of the low-energy absorption band. The calculated electronic transitions and the corresponding natural transition orbitals (Figures S1–S5) are consistent with this interpretation, although they do not by themselves provide conclusive evidence for a charge-transfer excited state. Specific solvent–solute interactions

may further contribute to the observed spectral behavior, in agreement with previous reports on structurally related heterocyclic push–pull chromophores[20,21].

The UV–Vis spectra of **7**–**11** in various solvents reveal solvatochromism, influenced by the number of hydroxyl groups and imidazole nitrogen substitution (Fig. 2). Unsubstituted **7** displayed a hypsochromic shift in absorption maxima compared to other systems. Monohydroxy-substituted **8** showed a hypochromic shift in absorbance intensity accompanied by a bathochromic shift in absorption maxima relative to **7**. The dihydroxy-substituted **9** exhibited the most pronounced hyperchromic shift in absorbance intensity, while the addition of a third –OH group in **10** resulted in a further hypochromic shift in absorbance intensity with a slight bathochromic shift in absorption maxima. *N*3-methyl substitution in **11** induced both a hypochromic shift in absorbance intensity and a hypsochromic shift in absorption maxima relative to **10** across all solvents.

UV–Vis pH titrations

To assess the pH-sensing capabilities of **7**–**11**, UV–Vis titration experiments were conducted in buffer solutions at a concentration of 2×10^{-5} mol dm^{-3} across a pH range of 1 to 13. Figure 3 presents the absorption spectra of studied compounds at different pH values. While spectrophotometric titration enables direct monitoring of pH-dependent spectral evolution, theoretical spectra were computed to help assign the experimentally observed bands to the dominant protonation forms, particularly in **9**–**11** where several protolytic equilibria overlap within a narrow pH range. Unsubstituted **7** exhibited a bathochromic shift in absorption maxima accompanied by a hyperchromic shift in absorbance intensity in highly acidic conditions (pH 1–4). As the buffer pH increased, a hypochromic shift in absorbance intensity was observed, along with a further bathochromic shift in absorption maxima.

The introduction of –OH groups in **8**–**10** provided additional pH-responsive sites, leading to more varied spectral responses. For monohydroxy-substituted **8**, the highest absorbance intensity occurred in acidic conditions at pH 1 and 4. While intensity changes alone were insufficient to distinguish closely spaced pH values (e.g., pH 3–7, with absorbance differing by < 10%), significant bathochromic shifts (e.g., 56 nm from pH 7 to

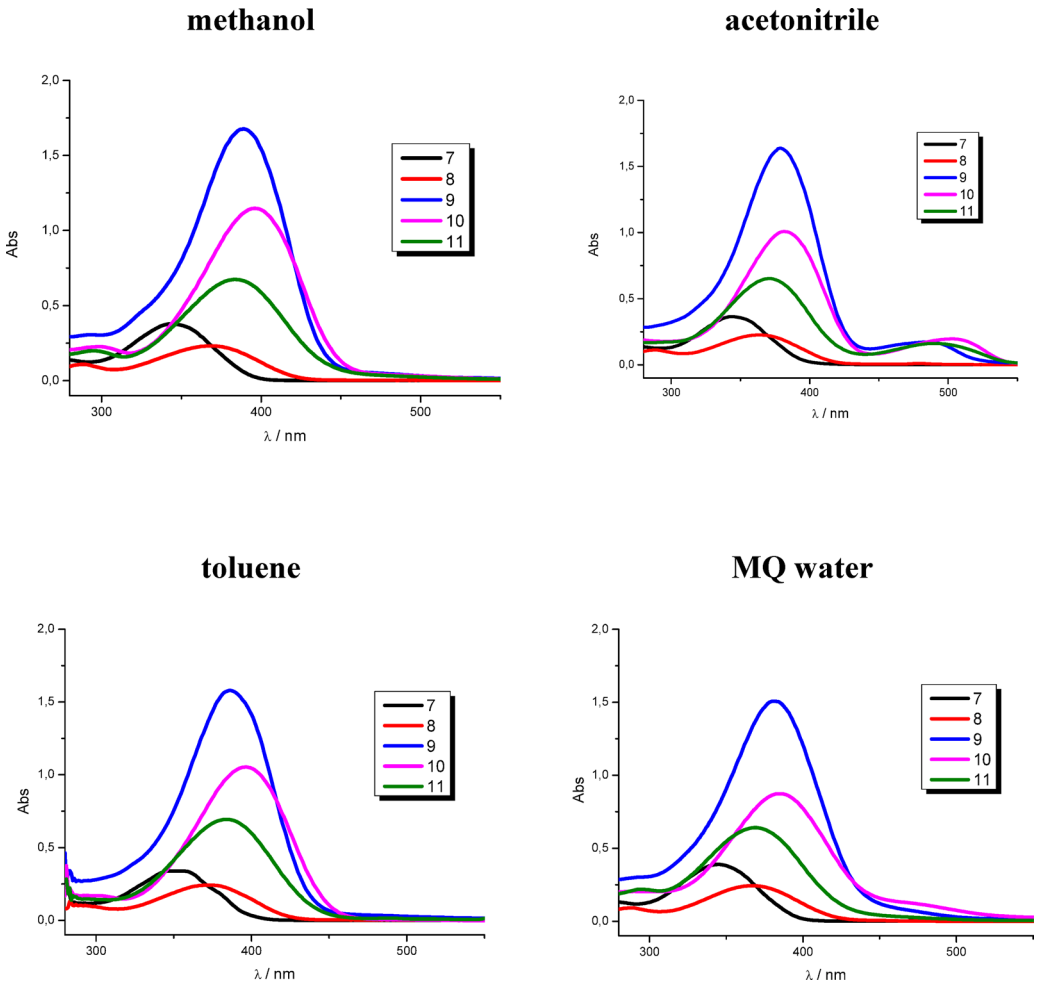

Fig. 2. Comparative UV–Vis absorption spectra of **7**–**11** in representative solvents ($c \approx 2 \times 10^{-5}$ mol dm^{-3}), overlaid to highlight substituent effects on peak positions and relative intensities (e.g., hypsochromic progression from **7** to **11**). Solvents are grouped by representative polarity classes rather than strict $E_T(30)$ order for visual clarity; compounds appear in the same sequence as in Fig. 1.

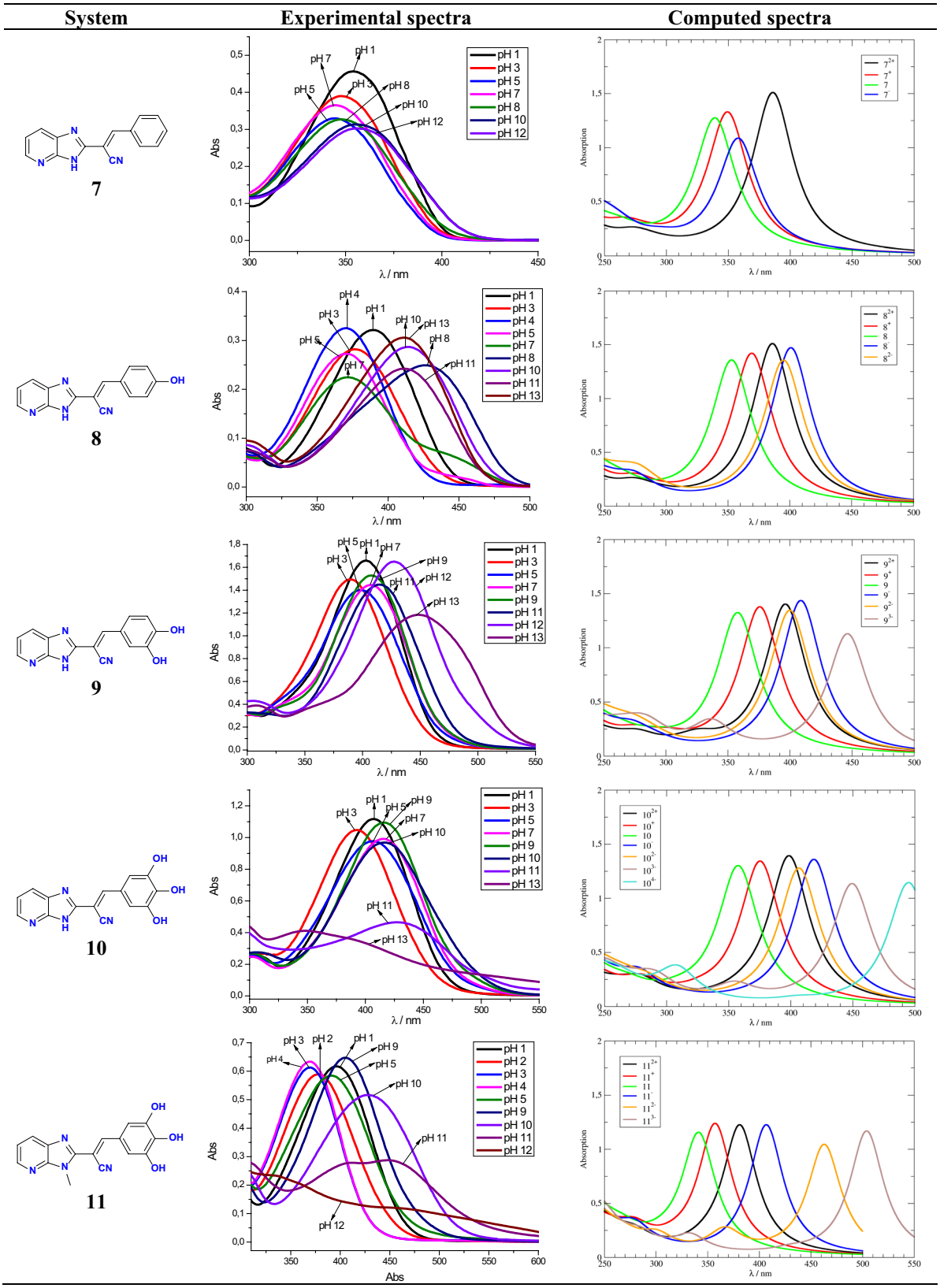

Fig. 3. Absorption spectra of **7**–**11** in buffers of different pH values, recorded at $c \approx 2 \times 10^{-5}$ mol dm^{-3}, together with TD-DFT simulated spectra used to assign the experimentally observed transitions to individual protonation forms, with computed absorption maxima showing agreement within 5–15 nm of experimental values. Colorimetric responses to changes in solution pH values are photographed in Figure S6.

8) enabled clear visual or ratiometric detection of neutral-to-basic transitions. Estimated limits of detection, calculated as 3σ/slope from titration curves, ranged from 0.2 to 0.5 pH units near the compounds' pK_a values, indicating potential for targeted pH-sensing applications despite some overlap. Importantly, such behavior illustrates the limitations of relying solely on experimental spectra for systems with multiple closely spaced pK_a values. In this context, the integration of TD-DFT calculations proved essential, as it enabled deconvolution of overlapping absorption bands and assignment of individual spectral contributions to specific protonation states. This combined approach provides a level of mechanistic insight that extends beyond routine spectrophotometric analysis and is particularly valuable for complex multi-equilibria systems.

For **8**, a hypochromic shift in absorbance intensity was seen up to pH 5, with intensity increasing again from pH 8, accompanied by a pronounced bathochromic shift with absorption maxima at 427 nm. At pH 7, **8** showed the lowest absorbance intensity with a slight hypsochromic shift, with maxima at 371 nm. Dihydroxy-substituted **9** showed the highest absorbance intensity at extreme pH values (pH 1 and 12), with intensity decreasing as pH increased from 1 to 12, followed by a hypsochromic shift. At pH 13, the lowest absorbance intensity was observed with a significant bathochromic shift at 448 nm, while at pH 3, a hypsochromic shift occurred at 389 nm. Trihydroxy-substituted **10** exhibited the highest absorbance intensity at pH 1, which decreased with increasing pH. At pH 3, a hypsochromic shift was observed with maxima at 392 nm, while in basic conditions at pH 11, a hypochromic shift occurred with a significant bathochromic shift at 429 nm.

*N*3-methyl substitution in **11**, which also bears three hydroxyl groups, altered the spectral response, confirming the critical role of the unsubstituted N–H group in pH sensing. Compound **11** showed the highest absorbance intensity at pH 9 with a bathochromic shift in absorption maxima at 405 nm. In more basic conditions (pH 10–12), absorbance intensity decreased. At pH 11, two absorption maxima were observed at 408 nm and 451 nm, suggesting possible dual protonation states. In acidic conditions, a hypsochromic shift was noted, most pronounced at pH 3 with maxima at 369 nm.

The observed spectral behavior highlights the inherent limitations of purely experimental analysis in systems with multiple closely spaced protonation equilibria. In such cases, the integration of TD-DFT calculations proved essential for interpreting the UV–Vis response, as it enabled reliable assignment of overlapping absorption features to specific protonation forms. This was particularly important for compounds **9**–**11**, where several equilibria occur within a narrow pH window, leading to complex spectral profiles that cannot be unambiguously resolved based on experimental data alone.

Computational DFT analysis

We used computational DFT analysis to identify the predominant protonation forms of each system that drive changes in photophysical responses under varying pH conditions. The B3LYP/6–311++G(2df,2pd)//(SMD)/B3LYP/6–31+G(d) model calculated aqueous-phase pK_a values (Table 2), while the (SMD)/CAM-B3LYP/6–31+G(d)//(SMD)/B3LYP/6–31+G(d) approach predicted UV–Vis spectra for each protonation form (Fig. 3). A systematic comparison between computed and experimental absorption maxima shows consistent agreement within 5–15 nm across all investigated protonation states, confirming that the selected computational protocol reliably captures the key electronic transitions. Importantly, this level of agreement enables direct assignment of experimentally observed absorption bands to specific protonation forms, even in cases where multiple equilibria overlap.

The studied molecules feature an imidazo[4,5-*b*]pyridine core linked to phenyl and hydroxy-substituted phenyl moieties via an acrylonitrile bridge. In this context, it is worth mentioning the experimental pK_a values for model systems relevant for the present analysis. The unsubstituted imidazo[4,5-*b*]pyridine is only moderately basic heterocycle (p$K_a \approx 4$–5) with the pyridine nitrogen as the preferred protonation site[22]. This is due to its sp^2-hybridized lone pair, which is more available for protonation compared to the imidazole nitrogen, where the lone pair is partially delocalized in the aromatic system. This contrasts with the lower basicity of pyridine (p$K_a = 5.23$) over imidazole (p$K_a = 6.95$),[22] being a consequence of different responses of these simple systems towards the π-network extension. In contrast, phenol deprotonation typically occurs at pH ≈ 10, and can be expected in our experiments. Moreover, additional –OH groups further increase acidity (p$K_a = 9.99$ for 4-phenol, 9.40 for 3,4-dihydroxy, 8.55 for the 3,4,5-trihydroxy derivative)[23]. All of this indicates the importance of the –OH deprotonation in our case, especially knowing that imidazole deprotonation requires higher basicities (p$K_a = 14.5$),[22] making it less relevant under our conditions.

The relative stabilities of the possible *N*1, *N*3 and *N*4 tautomers of compounds **7**–**10** in their neutral, monoprotonated and monodeprotonated forms were also examined. The results (Table S1) show that the *N*1 tautomer is preferred in the large majority of cases; the only exceptions are neutral **7** and monodeprotonated **9**, for which the *N*3 form is lower in energy. All subsequent computational data reported in this work refer to the lowest-energy tautomer of each protonation state.

Molecule **7**, the simplest system, consists of a plain imidazo[4,5-*b*]pyridine core linked to an unsubstituted phenyl group. The most basic position belongs to the pyridine nitrogen, with a computed pK_a of 2.3, closely matching the experimental value of 2.4. According to our calculations, this site is favored over the imidazole nitrogen by 3.1 kcal mol^{-1}, rendering the later much less abundant and negligible for our analysis. Such a basicity is significantly lower than that of the parent imidazo[4,5-*b*]pyridine, predominantly due to the unfavorable extension of the π-network, coupled with the presence of the strong electron-withdrawing –CN group, known for its significant basicity reduction effect[24,25]. All of this indicates that under normal conditions **7** remains unionized in the aqueous solution.

The UV–Vis spectra of molecule **7** confirms its protonation behavior. The computed absorption maximum for neutral **7** at 339 nm aligns with 344 nm measured at pH = 7, while 349 nm for protonated 7^+ matches 354 nm at pH = 1. According to the computed p$K_a = -5.7$, further protonation at the imidazole nitrogen is unlikely, as the computed 386 nm absorption for 7^{2+} is absent experimentally. On the other hand, **7** contains only one acidic

Compound	Protonation Forms	Process	$pK_{a,CALC}$	$pK_{a,EXP}$
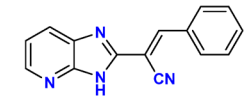	$\mathbf{7}^{+} \rightarrow \mathbf{7}^{2+}$	benzimidazole N protonation	–5.7	
	$\mathbf{7} \rightarrow \mathbf{7}^{+}$	pyridine N protonation	2.3	2.4
	$\mathbf{7} \rightarrow \mathbf{7}^{-}$	benzimidazole N–H deprotonation	12.3	
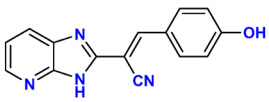	$\mathbf{8}^{+} \rightarrow \mathbf{8}^{2+}$	benzimidazole N protonation	–4.8	
	$\mathbf{8} \rightarrow \mathbf{8}^{+}$	pyridine N protonation	4.1	2.3
	$\mathbf{8} \rightarrow \mathbf{8}^{-}$	phenol *p*-OH deprotonation	7.3	7.0
	$\mathbf{8}^{-} \rightarrow \mathbf{8}^{2-}$	benzimidazole N–H deprotonation	15.4	
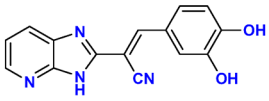	$\mathbf{9}^{+} \rightarrow \mathbf{9}^{2+}$	benzimidazole N protonation	–4.7	
	$\mathbf{9} \rightarrow \mathbf{9}^{+}$	pyridine N protonation	2.9	2.3
	$\mathbf{9} \rightarrow \mathbf{9}^{-}$	phenol *p*-OH deprotonation	6.1	6.7
	$\mathbf{9}^{-} \rightarrow \mathbf{9}^{2-}$	benzimidazole N–H deprotonation	12.3	10.6
	$\mathbf{9}^{2-} \rightarrow \mathbf{9}^{3-}$	phenol *m*-OH deprotonation	14.2	
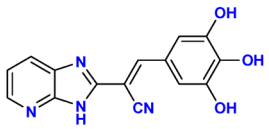	$\mathbf{10}^{+} \rightarrow \mathbf{10}^{2+}$	benzimidazole N protonation	–4.7	
	$\mathbf{10} \rightarrow \mathbf{10}^{+}$	pyridine N protonation	3.1	2.3
	$\mathbf{10} \rightarrow \mathbf{10}^{-}$	phenol *p*-OH deprotonation	4.4	4.2
	$\mathbf{10}^{-} \rightarrow \mathbf{10}^{2-}$	benzimidazole N–H deprotonation	12.5	10.2
	$\mathbf{10}^{2-} \rightarrow \mathbf{10}^{3-}$	phenol *m*-OH deprotonation	13.6	
	$\mathbf{10}^{3-} \rightarrow \mathbf{10}^{4-}$	phenol *m*-OH deprotonation	15.6	
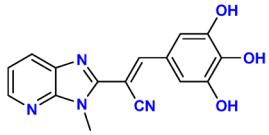	$\mathbf{11}^{+} \rightarrow \mathbf{11}^{2+}$	benzimidazole N protonation	–4.4	
	$\mathbf{11} \rightarrow \mathbf{11}^{+}$	pyridine N protonation	3.5	2.3
	$\mathbf{11} \rightarrow \mathbf{11}^{-}$	phenol *p*-OH deprotonation	5.5	6.0
	$\mathbf{11}^{-} \rightarrow \mathbf{11}^{2-}$	phenol *m*-OH deprotonation	12.1	11.3
	$\mathbf{11}^{2-} \rightarrow \mathbf{11}^{3-}$	phenol *m*-OH deprotonation	13.6	

Table 2. Calculated aqueous-phase pK_a values by the B3LYP/6–311++G(2df,2pd)//(SMD)/B3LYP/6–31+G(d) model and their comparison with experimental data reported in this work.

hydrogen – imidazole N–H group – and its acidity is estimated at $pK_a = 12.3$. The latter falls in the expected territory, as the acidity of the parent imidazole is $pK_a = 12.8$,[22] making the $\mathbf{7} \rightarrow \mathbf{7}^{-}$ transition only partly visible at high pH. Still, we note the shift in the measured transitions from 344 nm at pH = 7 to 356 nm at pH = 12, which is supported by the absorption maximum computed for $\mathbf{7}^{-}$ at 358 nm, confirming the experimental trend. As such, we can conclude that our experiments capture the transition between neutral and monoprotonated forms at $pK_a = 2.4$, while the matching deprotonation mostly resides outside the employed conditions and should dominate only as the pH exceeds 12.

Introducing a *para*-OH group in **8** alters its acid–base properties. Not so much in its basicity features, as the pyridine nitrogen remains the most basic site. Yet, the positive electron-donating effect of the added –OH group promotes the nitrogen basicity in this part of the molecule by 1.8 units up to $pK_a = 4.1$ through the resonance effect. We support this by noting the agreement between UV–Vis lines centered at 353 and 369 nm computed for **8** and $\mathbf{8}^+$, matching the values of 371 and 388 nm measured at pH = 7 and pH = 1, respectively. As expected, the newly present phenolic –OH group is much more acidic than imidazole N–H, with a computed pK_a of 7.3 well-matching the experimental 7.0. Moreover, the simulated UV–Vis spectra for $\mathbf{8}^-$ at 401 nm agrees with values around 412 nm measured for pH = 10–13. Such a substantial red shift of 41 nm in the $\mathbf{8} \rightarrow \mathbf{8}^-$ transition, occurring near neutral pH, positions **8** as a promising candidate for detecting pH changes from neutrality to higher values. Furthermore, imidazole deprotonation in $\mathbf{8}^-$ is energetically unfavorable, becoming significant only at pH > 15, and the absence of a 395 nm absorption line in the spectra, computed for $\mathbf{8}^{2-}$ at highest pH conditions, rules out the $\mathbf{8}^- \rightarrow \mathbf{8}^{2-}$ transition.

Adding one (molecule **9**) or two (molecule **10**) –OH groups to the phenyl moiety of molecule **8** moderately affects protonation but significantly enhances acidity. The pyridine nitrogen remains the preferred protonation site, with computed pK_a values of 2.9 for **9** and 3.1 for **10**, nicely matching experimental values 2.3 in both cases. These transitions are visible in the UV–Vis spectra, evident in the red shift from 389 nm (pH = 3) to 403 nm (pH = 1) in **9**, and also from 392 nm (pH = 3) to 407 nm (pH = 1) in **10**. Both of these trends are confirmed through computed transitions, assuming 358 nm for both **9** and **10**, and 376 nm for their monoprotonated forms $\mathbf{9}^+$ and $\mathbf{10}^+$. Further protonation of both systems again exceeds the employed conditions and is not considered.

The additional –OH groups lower the phenolic pK_a from 7.3 in **8** to 6.1 in **9** and 4.4 in **10**, driven by stabilizing O–H···O$^-$ hydrogen bonds – one in **9**, and two in **10**. Accordingly, the phenol acidity increases as **8** < **9** < **10**. A very significant consequence of these intramolecular hydrogen bonds is the fact that under normal conditions both **9** and **10** predominate as anions deprotonated at the phenol moiety. This is confirmed by observing that the computed absorption maxima for both **9** and **10** are at 358 nm, while for $\mathbf{9}^-$ and $\mathbf{10}^-$ are at 409 and 419 nm. Accordingly, the latter set of values are found in much closer agreement with measured values of 407 and 416 nm for **9** and **10** at pH = 7, thereby validating the predominance of monodeprotonated forms under neutral conditions.

Following that, the next most acidic site in both $\mathbf{9}^-$ and $\mathbf{10}^-$ is consistently the imidazole N–H, irrespective of the number of the –OH groups present. Computed pK_a values assume 12.3 and 12.5 for **9** and **10**, and are found in reasonable agreement with 10.6 and 10.2 measured experimentally. Given the overall success of our computational model in achieving much better agreement with other experimental pK_a values reported here, we believe a somewhat higher discrepancy among these values comes as a result of several interconnected acid–base processes occurring around the same pH value, which complicate experimental pK_a determination. Specifically, our DFT computations suggest that in **9**, the benzimidazole and second –OH deprotonation occur within 2 pK_a units, while in **10**, benzimidazole and two subsequent –OH deprotonations all take place within only 3 pK_a units. Nevertheless, the computed UV–Vis transitions are well-matched with measured data. For example, experimental spectra for **9** indicate absorption maxima at 408 nm (pH = 9) and a large red shift to 448 nm (pH = 13). According to the calculated pK_a values, at pH = 9 the system should be present as a deprotonated $\mathbf{9}^-$, for which the computed UV–Vis spectra at 409 nm ties in with experiments. Interestingly, the spectra computed for dideprotonated $\mathbf{9}^{2-}$ occurs at 400 nm, and this overlap likely prevents this form from being distinguishable in the spectra. In contrast, the UV–Vis absorption for trideprotonated $\mathbf{9}^{3-}$ appears at 446 nm, and this form is likely responsible for the highly blue-shifted line at 448 nm at pH = 13. Such a conclusion is supported by the computed pK_a value for the $\mathbf{9}^{2-} \rightarrow \mathbf{9}^{3-}$ transition of 14.2, which predicts around 10% population of trideprotonated $\mathbf{9}^{3-}$ at pH = 13.

Lastly, we focus on molecule **11**, an *N*3-methyl derivative of **10**. This subtle modification primarily affects its protonation, which increases the pK_a value by 0.4 units to 3.5. Although the numerical agreement is likely accidental, such a trend is consistent with *N*-methylimidazole's 0.4-unit higher basicity over imidazole. Nevertheless, this transition is well-supported by calculations, as the absorption lines at 357 nm for $\mathbf{11}^+$ and 341 nm for **11** agree with 377 nm at pH = 2 and 367 nm at pH = 4. Furthermore, **11** remains highly –OH acidic, so the obtained $pK_a = 5.5$ foresees the dominance of the deprotonated $\mathbf{11}^-$ at 3 < pH < 12. This ties in with the absorption maximum at 407 nm computed for $\mathbf{11}^-$ that matches 405 nm measured at pH = 9. Deprotonation of the remaining two –OH groups occurs at $pK_a = 12.1$ and 13.6, aligning with an experimental pK_a of 11.3, reflecting closely spaced acid–base processes.

The multi-step acid–base equilibria contribute to complex, overlapping absorption bands in experimental spectra, potentially limiting direct interpretability. However, DFT-predicted spectra for individual protonation forms enable deconvolution, revealing distinct contributions (e.g., pyridine protonation causing 10–20 nm red shifts in acidic pH). In practical applications, this complexity can be addressed via ratiometric sensing at select wavelengths (e.g., monitoring 370/420 nm ratios for **8**) or multivariate analysis, enhancing utility despite broad bands. The absence of clear isosbestic points in the experimental pH titrations is consistent with the coexistence of several protonation (and, in a few cases, tautomeric) forms whose populations change with pH; the calculated pK_a values and TD-DFT spectra of the dominant lowest-energy species nevertheless permit reliable band assignment (Fig. 3).

Across molecules **7**–**11**, DFT calculations reveal that pyridine nitrogen protonation governs behavior at low pH, while phenolic –OH deprotonation drives spectral shifts at neutral to high pH. Additional –OH groups enhance acidity via hydrogen bonding, with molecules **9**, **10**, and **11** existing as anions under neutral conditions. The computational models achieve very good agreement with experimental pK_a and UV–Vis data, providing a robust framework for envisaging pH-dependent photophysical properties of imidazo[4,5-*b*]pyridine derivatives. These insights are valuable for designing pH-sensitive fluorescent probes or optoelectronic materials. Overall, the combined experimental–computational analysis provides a coherent mechanistic picture of pH-dependent

	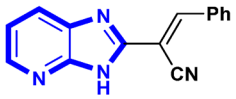 Imidazo[4,5-*b*]pyridine unit	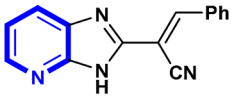 Pyridine part	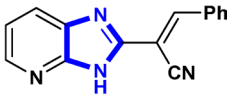 Imidazole part
7 neutral	–0.03 |e|	0.23 |e|	0.21 |e|
7^+ protonated at pyridine	0.92 |e|	1.10 |e|	0.39 |e|
7^+ protonated at imidazole	0.87 |e|	0.40 |e|	0.99 |e|

Fig. 4. Charge distribution in molecule **7**, in its neutral or protonated forms at either the pyridine or imidazole nitrogen, as determined by NBO analysis using the SMD/HF/6–31 + G(d) model in water. Considered atoms, including attached hydrogens, are highlighted in bold blue.

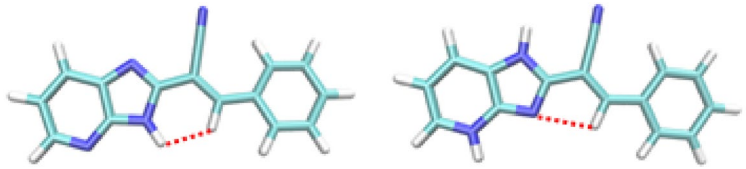

Fig. 5. Changes in the molecular geometry following the pyridine protonation under acidic conditions with a focus on the acrylonitrile unit, taking **7** as an illustrative example, obtained at the (SMD)/B3LYP/6–31+G(d) level of theory in water.

behavior across the studied series, revealing how subtle structural modifications govern protonation pathways, charge distribution, and optical response. Importantly, this approach enables prediction of dominant species under specific conditions and rationalization of spectral trends, thereby establishing a framework that can be applied to the design of related pH-responsive chromophores.

NMR measurements

Investigated compounds **7**–**11** were subjected to NMR analysis with the aim of determining the site of protonation in acidic conditions, especially given the closely spaced basicities of pyridine and imidazole nitrogens within the imidazo[4,5-*b*]pyridine core. For each molecule, a pair of samples was prepared: one under slightly basic conditions (approximately pH* ≈ 8) and the other under highly acidic conditions (approximately pH* ≈ 2), using 90:10 DMSO-d_6:D_2O mixtures for solubility[26]. Proton and carbon chemical shifts were recorded under both conditions and compared, as summarized in Table S2. Note that pH* values represent approximate effective pH scales, estimated from aqueous-calibrated electrode readings with a standard 0.4-unit pD-to-pH correction; in DMSO-dominant media, minor offsets (± 0.5 units) may arise due to altered electrode response, but these do not impact qualitative Δδ trends.

For systems **7**–**10**, the largest proton chemical shift differences were consistently observed in the pyridine core, specifically at H-7, H-6, and H-5 (Δδ > 0.3 ppm), suggesting protonation occurs within this structural unit. This is supported by the computational charge distribution analysis of the imidazo[4,5-*b*]pyridine unit following protonation on either of its nitrogen atoms (Fig. 4). Before protonation, the unit is nearly neutral, with each fragment carrying approximately one-fifth of the positive charge due to the cumulative positive charge on the bridging carbons. Upon pyridine protonation, about 0.05 |e| larger amount of excess positive charge remains in the bicyclic core, while imidazole protonation redistributes this charge to the rest of the system via resonance. Notably, pyridine protonation concentrates 87% of the excess positive charge in its 6-membered ring, compared to only 17% for imidazole protonation. This supports the conclusion that chemical shift changes in the pyridine core arise from its nitrogen protonation, consistent with DFT free energy differences (> 3 kcal mol^{-1} favoring pyridine site).

We also observed significant changes in the proton chemical shift of the acrylonitrile H-13. These changes are not due to protonation but result from altered molecular geometry following proton attachment to the pyridine nitrogen. At pH* ≈ 8, in all four compounds, neutral (**7** and **8**) or monodeprotonated ($\mathbf{9}^-$ and $\mathbf{10}^-$), H-13 is oriented toward the imidazole N–H group (Fig. 5), with H···H distances of 2.11 Å (**7**), 2.09 Å (**8**), 2.05 Å ($\mathbf{9}^-$), and 2.06 Å ($\mathbf{10}^-$). In contrast, at pH* ≈ 2, pyridine nitrogen protonation alters the molecular geometry,

causing H-13 to point toward the unsaturated imidazole nitrogen, with N···H distances of 2.46 Å in all four systems. This environmental change around H-13 accounts for its chemical shift alterations upon pH reduction. Similarly, carbon chemical shifts show the most significant changes at pyridine positions C-2, C-5, and C-6, and acrylonitrile-linked C-13 and C-10. All of these findings indicate that pyridine protonation is the dominant site, consistent with computational results.

In contrast, **11**, with a methyl group on the imidazole nitrogen, showed a somewhat distinct pattern. Proton chemical shifts varied uniformly across the spectrum, providing no clear indication of a specific protonation site. However, carbon chemical shifts exhibited significant changes at C-8, C-10, and C-13, suggesting contributions from both pyridine and imidazole protonation sites. This is attributed to compound **11** having the smallest energy difference between its protonation tautomers. Unlike **7**–**10**, where pyridine protonation is strongly favored by Gibbs free energy differences of 3.1 (**7** and **8**), 3.3 (**10**), and as much as 4.0 kcal mol^{-1} (**9**), compound **11** has a difference of only 1.9 kcal mol^{-1}. Although pyridine protonation remains preferred, such an energy margin indicates approximately 4% of the population exists as the imidazole-protonated tautomer, explaining the observed trends in chemical shifts.

Conclusion

Imidazo[4,5-*b*]pyridine acrylonitrile derivatives **7**–**11** demonstrate significant potential as pH sensors, with tunable spectroscopic properties enabling precise detection across a wide pH range (1–13). While spectral overlaps and moderate bathochromic shifts (e.g., 10–56 nm) may complicate broadband absorption-based sensing, these challenges can be addressed through ratiometric analysis or integration with emission properties, as observed in similar heterocyclic push–pull chromophores. The strategic incorporation of hydroxyl groups significantly enhanced pH sensitivity, particularly in dihydroxy-substituted **9** and trihydroxy-substituted **10**, which exhibited pronounced bathochromic shifts due to increased phenolic acidity of the hydroxyl groups on the phenyl core. Notably, monohydroxy-substituted **8** proved promising for monitoring neutral-to-basic transitions, with a significant bathochromic shift (e.g., 56 nm from pH 7 to 8) in UV–Vis spectra, making it suitable for detecting subtle alkalinity changes in applications such as environmental monitoring.

The unsubstituted N–H group on the imidazo[4,5-*b*]pyridine core was critical for pH sensing, as evidenced by the altered spectral response of *N*3-methyl-substituted **11**, which lacks the free N–H group. UV–Vis titrations, supported by computational DFT and NMR analyses, confirmed the pyridine nitrogen as the primary protonation site and highlighted the role of hydroxyl groups in modulating acid–base properties. These findings establish compounds **7**–**11** as versatile pH sensors while, more importantly, providing generalizable design principles for tuning pH responsiveness in conjugated heterocyclic systems. The present study demonstrates that hydroxyl substitution and N–H functionality act cooperatively to control acidity, protonation pathways, and intramolecular charge transfer, thereby enabling predictable modulation of optical properties.

A key outcome of this work is the demonstration that combined UV–Vis spectroscopy and TD-DFT analysis can successfully deconvolute overlapping protonation equilibria, allowing reliable assignment of spectral features even in complex multi-state systems. This represents an important step beyond conventional spectroscopic studies, where such overlaps often limit mechanistic interpretation. In this context, compound **8** is identified as a particularly promising probe for neutral-to-basic pH transitions, addressing a sensing range that is less frequently optimized in related systems. More broadly, the insights gained here provide a rational framework for the design of next-generation optical pH sensors and functional chromophores, with potential applications in environmental monitoring, biomedical diagnostics, and optoelectronic materials.

Experimental part

Spectroscopic Characterization

A Varian Cary 50 spectrophotometer in double-beam mode was used to record the UV–Vis absorption spectra in organic solvents of reagent grade in the wavelength range of 200–550 nm at room temperature. The absorbance values were recorded with a 0.1 nm resolution using transparent quartz cuvettes of 1 cm path length.

pH Titrations

To study the changes in the spectroscopic characteristics of acrylonitriles **7**–**11** obtained within the usage of reagent-grade universal buffers with different pH values within pH = 1–13, room-temperature UV–Vis spectra were recorded. Amounts of 0.1 M pH buffer solutions were prepared using boric acid, citric acid, phosphoric acid and sodium hydroxide, and pH was adjusted with hydrochloric acid. As terminal acidic and basic points in the titration experiments, solutions of 0.1 mol dm^{-3} hydrochloric acid (for pH = 1) and 0.1 mol dm^{-3} sodium hydroxide (for pH = 13) were used. The employed concentrations of acrylonitriles **7**–**11** were 2×10^{-5} mol dm^{-3} for UV–Vis measurements. The pK_a values were determined using a Mettler Toledo FiveEasy pH meter F20, calibrated using the three-point method with standard aqueous buffers of pH 4.00, 7.00, and 10.00. The compounds were initially dissolved in DMSO and subsequently diluted with 0.1 M KCl to obtain a final concentration of 2.5×10^{-5} M. The ionic strength of the solution was maintained constant using 0.1 M KCl. 15 mL of the compound solution in 0.1 M KCl was acidified with 0.1 M HCl, and potentiometric titration was then carried out by incremental addition of 0.1 M NaOH until the pH reached 12.0–12.5 and stabilized. All measurements were conducted at a constant temperature of 25 °C, after a stabilization period of 2–3 min prior to recording[27]. Equivalence points were determined using OriginPro 2018 by fitting the titration curves with a Boltzmann sigmoidal function, and the corresponding inflection points were extracted to obtain the pK_a values (Figures S7–S11).

NMR measurement

For measurements under slightly basic conditions: 4950 µL of DMSO-d_6 was mixed with 550 µL of D_2O, resulting in an approximate pD of 8.1. After applying a correction of 0.4 units to account for the change in glass electrode potential due to D_2O, the effective pH* was estimated to be 8.5 (with potential ± 0.5 unit offset in DMSO-dominant media). Aliquots of 700 µL from this solution were used to dissolve 4.8 mg (**7**), 9.6 mg (**8**), 8.9 mg (**9**), 10.6 mg (**10**) and 10.5 mg (**11**), resulting in adjusted pH* values of 8.4 (**7**), 8.5 (**8**), 8.7 (**9**), 8.7 (**10**) and 8.1 (**11**). For measurements under acidic conditions: 4950 µL of DMSO-d_6 was mixed with 550 µL of 1 M DCl in D_2O, resulting in an approximate pD of 1.5. After correcting for the glass electrode potential by 0.4 units, effective pH* was estimated to be 1.9 (with potential ± 0.5 unit offset). Compounds **7**–**11** were individually added to 700 µL aliquots of this solution at the following quantities: 5.2 mg (**7**), 10.4 mg (**8**), 11.1 mg (**9**), 9.4 mg (**10**) and 9.5 mg (**11**). The resulting pH* values were 2.0 (**7**), 2.1 (**8**), 2.1 (**9**), 2.1 (**10**) and 2.0 (**11**). The complete ^{1}H and ^{13}C assignments were established using one- and two-dimensional NMR spectra (^{1}H, ^{13}C, COSY, HSQCe and HMBC), recorded on a Bruker Avance AV600 spectrometer equipped with a 5 mm BBO probe and z-gradient accessory employing standard Bruker pulse sequences (Bruker, Billerica, USA). More experimental details can be found in the Supplementary Information. All pH measurements were conducted using a Metrohm 827 pHlab pH-meter with a 6.0234.100 electrode (Metrohm, Herisau, Switzerland). All deuterated solvents were purchased from EurIsotop, Saint-Aubin, France. The NMR data was processed using various versions of TopSpin (Bruker, Billerica, USA) and MNova 15.1 (Mestrelab Research, Santiago de Compostela, Spain) software packages.

Computational details

All molecular geometries were optimized using the B3LYP/6–31+G(d) level of theory, which is widely recognized as providing a reliable balance between accuracy and computational cost for organic π-conjugated systems. Hybrid functionals such as B3LYP, in combination with polarized and diffuse basis sets, have been extensively validated for predicting molecular geometries and electronic structure of heteroaromatic compounds. Moreover, benchmark studies have shown that TD-DFT calculations based on B3LYP geometries typically reproduce experimental UV–Vis absorption maxima with reasonable accuracy, particularly when solvation effects are included, making this approach suitable for spectroscopic investigations[28,29]. Electronic energies were supplemented with thermal corrections from unscaled frequency calculations, ensuring that all reported values correspond to Gibbs free energies at room temperature and standard pressure. Gas-phase energies were refined with single-point calculations using the more flexible 6–311++G(2df,2pd) basis set. The solvent environment was modeled using the SMD continuum model for water, yielding the B3LYP/6–311++G(2df,2pd)//(SMD)/B3LYP/6–31+G(d) approach employed here. The continuum SMD solvent model was employed throughout. While the inclusion of explicit water molecules can further improve the description of localized hydrogen bonding in anionic states, such microsolvation was not pursued systematically because of the substantial increase in computational cost associated with conformational sampling across multiple protonation forms of five compounds. The present protocol already yields pK_a values and absorption maxima in good agreement with experiment (Table 2 and Fig. 3), which is sufficient for the assignment of dominant species and spectral features under the investigated conditions. This computational setup was justified by its success in reproducing kinetic and thermodynamic data for organic[30] and biochemical[31] processes, as well as pK_a values for similar organic derivatives[32,33]. pK_a values were calculated using an absolute method, incorporating the gas-phase free energy of a proton, $G(H^+) = 6.28$ kcal mol^{-1}, and its experimental aqueous-phase solvation free energy, $\Delta G_{SOLV}(H^+) = -265.9$ kcal mol^{-1},[34] consistent with the value used by Truhlar et al.[35] in parameterizing the SMD model. This solvation energy includes a free energy contribution of –1.89 kcal mol^{-1} to account for the transition from a gas-phase pressure of 1 atm to a liquid-phase concentration of 1 M. UV–Vis electronic transitions were calculated using the (SMD)/CAM-B3LYP/6–31+G(d) single-point calculations with the TD-DFT approach, considering the 32 lowest-energy singlet electronic excitations, in line with our earlier reports on similar systems.[32,36] All calculations were performed using the Gaussian 16 suite of programs[37].

Data availability

The data supporting this article have been included as part of the Supplementary Information.

Received: 25 June 2026; Accepted: 27 August 2026
Published online: 01 September 2026

References

1. Mandal, J. et al. An aminoquinoline based biocompatible fluorescent and colourimetric pH sensor designed for cancer cell discrimination. *New J. Chem.* **42**, 19818–19826.(2018). https://doi.org/10.1039/C8NJ04753G
2. Di Costanzo, L. & Panunzi, B. Visual pH Sensors: From a Chemical Perspective to New Bioengineered Materials. *Molecules* **26**, 2952. (2021). https://doi.org/10.3390/molecules26102952
3. Chen, W., Ma, X., Chen, H., Liu, S. H. & Yin, J. Fluorescent probes for pH and alkali metal ions. *Coord. Chem. Rev.* **427**, 213584. (2021). https://doi.org/10.1016/j.ccr.2020.213584
4. Wu, Z. et al. Organogelation of cyanovinylcarbazole with terminal benzimidazole: AIE and response for gaseous acid. *RSC Adv.* **6**, 97293–97301. https://doi.org/10.1039/C6RA20910F (2016).
5. Peng, J. et al. H-Bonding and C-H··· π assisted mechanofluorochromism of triphenylamine-containing vinylheterocycles bearing cyano and methyl groups. *New J. Chem.* **42**, 18269–18277. https://doi.org/10.1039/C8NJ03510E (2018).
6. Zhu, L. & Zhao, Y. Cyanostilbene-based intelligent organic optoelectronic materials. *J. Mater. Chem. C* **1**, 1059–1065. https://doi.org/10.1039/C2TC00593J (2013).
7. Suntsova, P. O. et al. Design and synthesis of disubstituted and trisubstituted thiazoles as multifunctional fluorophores with large Stokes shifts. *Dyes Pigm.* **166**, 60–71. https://doi.org/10.1016/j.dyepig.2019.02.051 (2019).

8. Zhang, Y., Huang, J., Kong, L., Tian, Y. & Yang, J. Two novel AIEE-active imidazole/α-cyanostilbene derivatives: photophysical properties, reversible fluorescence switching, and detection of explosives. *CrystEngComm* **20**, 1237–1244. https://doi.org/10.1039/C7CE01842H (2018).
9. Gao, L. et al. A robust, GFP-orthogonal photoswitchable inhibitor scaffold extends optical control over the microtubule cytoskeleton. *Chem. Cell. Biol.* **28**, 228–241. https://doi.org/10.1016/j.chembiol.2020.11.007 (2021).
10. Unsal Tan, O. & Zengin, M. Insights into the chemistry and therapeutic potential of acrylonitrile derivatives. *Arch. Pharm.* **255**, 2100383. https://doi.org/10.1002/ardp.202100383 (2022).
11. Horak, E. et al. Benzimidazole acrylonitriles as multifunctional push-pull chromophores: Spectral characterisation, protonation equilibria and nanoaggregation in aqueous solutions. *Spectrochim. Acta A Mol. Biomol. Spectrosc.* **178**, 225–233. https://doi.org/10.1016/j.saa.2017.02.011 (2017).
12. An, B.-K., Gierschner, J. & Park, S. Y. π-Conjugated cyanostilbene derivatives: A unique self-assembly motif for molecular nanostructures with enhanced emission and transport. *Acc. Chem. Res.* **45**, 544–554. https://doi.org/10.1021/ar2001952 (2012).
13. Kumar, G., Gupta, N., Paul, K. & Luxami, V. Acrylonitrile embedded benzimidazole-anthraquinone based chromofluorescent sensor for ratiometric detection of CN− ions in bovine serum albumin. *Sens. Actuators B Chem.* **267**, 549–558. https://doi.org/10.1016/j.snb.2018.04.071 (2018).
14. Jana, P., Yadav, M., Kumar, T. & Kanvah, S. Benzimidazole-acrylonitriles as chemosensors for picric acid detection. *J. Photochem. Photobiol. A Chem.* **404**, 112874. https://doi.org/10.1016/j.jphotochem.2020.112874 (2021).
15. Anandhan, K. et al. Solvatochromism and pH effect on the emission of a triphenylimidazole-phenylacrylonitrile derivative: experimental and DFT studies. *RSC Adv.* **9**, 12085. https://doi.org/10.1039/C9RA01275C (2019).
16. Boček, I. et al. Imidazo[4,5-*b*]pyridine derived tubulin polymerization inhibitors: Design, synthesis, biological activity *in vitro* and computational analysis. *Bioorg. Chem.* **127**, 106032. (2022). https://doi.org/10.1016/j.bioorg.2022.106032
17. Perin, N. et al. *N*-substituted benzimidazole acrylonitriles as *in vitro* tubulin polymerization inhibitors: Synthesis, biological activity and computational analysis. *Eur. J. Med. Chem.* **211**, 113003. (2021). https://doi.org/10.1016/j.ejmech.2020.113003
18. Beč, A. et al. Synthesis, computational analysis, and antiproliferative activity of novel benzimidazole acrylonitriles as tubulin polymerization inhibitors: Part 2. *Pharmaceuticals* **14**, 1052. https://doi.org/10.3390/ph14101052 (2021).
19. Boček Pavlinac, I. et al. Novel acrylonitrile derived imidazo[4,5-*b*]pyridines as antioxidants and potent antiproliferative agents for pancreatic adenocarcinoma. *Int. J. Biol. Macromol.* **266**, 131239. (2024). https://doi.org/10.1016/j.ijbiomac.2024.131239
20. Salehi, S., Memarian, H. R. & Sabzyan, H. Intramolecular charge transfer and locally excited state observation in push-pull 1, n-Bis (4-formylphenoxy) alkanes. *ACS Omega* **10**, 19705–19713. https://doi.org/10.1021/acsomega.5c00766 (2025).
21. Pounder, A. et al. Photobasicity-triggered twisted intramolecular charge transfer of push-pull chromophores. *J. Phys. Chem. B* **129**, 8485–8493. https://doi.org/10.1021/acs.jpcb.5c03367 (2025).
22. Tshepelevitsh, S. et al. On the Basicity of Organic Bases in Different Media. *Eur. J. Org. Chem.* **40**, 6735–6748. (2019). https://doi.org/10.1002/ejoc.201900956
23. Ackermann, G., Hesse, D. & Volland, P. Über Eisen(III)-Komplexe mit Phenolen. IV. Säurekonstanten einiger Polyphenole. *Z. Anorg. Allg. Chem.* **377**, 92–99. https://doi.org/10.1002/zaac.19703770111 (1970).
24. Vianello, R. & Maksić, Z. B. Towards highly powerful neutral organic superacids—a DFT study of some polycyano derivatives of planar hydrocarbons. *Tetrahedron* **61**, 9381–9390. https://doi.org/10.1016/j.tet.2005.07.052 (2005).
25. Vianello, R. & Maksić, Z. B. High acidity of polycyano azatriquinanes—theoretical prediction by the DFT calculations. *Tetrahedron Lett.* **46**, 3711–3713. https://doi.org/10.1016/j.tetlet.2005.03.142 (2005).
26. Yang, R. & Schulman, S. G. An operational pH in aqueous dimethylsulfoxide based upon the acidity dependence of the rate of a simple ionic recombination reaction in the lowest excited singlet state. *Talanta* **60**, 535–542. https://doi.org/10.1016/S0039-9140(03)00112-7 (2003).
27. Subirats, X., Fuguet, E., Rosés, M., Bosch, E. & Ràfols, C. Methods for pKa determination (I): Potentiometry, spectrophotometry, and capillary electrophoresis. *Mol. Sci. Chem. Eng.* (2015). https://doi.org/10.1016/B978-0-12-409547-2.11559-8
28. Khadiri, A. et al. DFT and TD-DFT calculations to estimate the photovoltaic parameters of some metal-free dyes based on triphenylamine: the influence of inserting an auxiliary electron-withdrawing group on DSSC's performance. *RSC Adv.* **15**, 26807–26829. (2025). https://doi.org/10.1039/D5RA04785D
29. Amorim, G. G. S., Homem-de-Mello, P. & Custodio, R. TD-DFT evaluation of electronic spectra of coumarin and anthraquinone dyes: Effects of functionals, basis sets, and solvation conditions. *ACS Omega* **11**, 5913–5920 (2026). https://doi.org/10.1021/acsomega.5c10203
30. Toma, M. et al. Transacylation in Ferrocenoyl-Purines. NMR and Computational Study of the Isomerization Mechanism. *J. Org. Chem.* **84**, 12471–12480. (2019). https://doi.org/10.1021/acs.joc.9b01944
31. Tandarić, T. & Vianello, R. Computational insight into the mechanism of the irreversible inhibition of monoamine oxidase enzymes by the antiparkinsonian propargylamine inhibitors rasagiline and selegiline. *ACS Chem. Neurosci.* **10**, 3532–3542. https://doi.org/10.1021/acschemneuro.9b00147 (2019).
32. Beč, A., Vianello, R. & Hranjec, M. Synthesis and spectroscopic characterization of multifunctional D-π-A benzimidazole derivatives as potential pH sensors. *J. Mol. Liq.* **386**, 122493. https://doi.org/10.1016/j.molliq.2023.122493 (2023).
33. Boček, I., Hranjec, M. & Vianello, R. Imidazo[4,5-*b*]pyridine derived iminocoumarins as potential pH probes: Synthesis, spectroscopic and computational studies of their protonation equilibria. *J. Mol. Liq.* **355**, 118982. (2022). https://doi.org/10.1016/j.molliq.2022.118982
34. Tissandier, M. D. et al. The proton's absolute aqueous enthalpy and Gibbs free energy of solvation from cluster-ion solvation data. *J. Phys. Chem. A* **102**, 7787–7794. https://doi.org/10.1021/jp982638r (1998).
35. Marenich, A. V., Cramer, C. J. & Truhlar, D. G. Universal solvation model based on solute electron density and on a continuum model of the solvent defined by the bulk dielectric constant and atomic surface tensions. *J. Phys. Chem. B* **113**, 6378–6396. https://doi.org/10.1021/jp810292n (2009).
36. Tolić Čop, K., Pranjić, M., Vianello, R., Stražić Novaković, D. & Mutavdžić Pavlović, D. Elimination of torasemide from aqueous medium: Influence of sorption and photocatalytic processes parameters supported by DFT analysis. *Environ. Sci. Pollut. Res.* **31**, 63176–63194. https://doi.org/10.1007/s11356-024-35356-6 (2024).
37. M. J. Frisch, G. W. Trucks, H. B. Schlegel, G. E. Scuseria, M. A. Robb, J. R. Cheeseman, G. Scalmani, V. Barone, G. A. Petersson, H. Nakatsuji, X. Li, M. Caricato, A. V. Marenich, J. Bloino, B. G. Janesko, R. Gomperts, B. Mennucci, H. P. Hratchian, J. V. Ortiz, A. F. Izmaylov, J. L. Sonnenberg, D. Williams-Young, F. Ding, F. Lipparini, F. Egidi, J. Goings, B. Peng, A. Petrone, T. Henderson, D. Ranasinghe, V. G. Zakrzewski, J. Gao, N. Rega, G. Zheng, W. Liang, M. Hada, M. Ehara, K. Toyota, R. Fukuda, J. Hasegawa, M. Ishida, T. Nakajima, Y. Honda, O. Kitao, H. Nakai, T. Vreven, K. Throssell, J. A. Montgomery, J. E. Peralta, F. Ogliaro, M. J. Bearpark, J. J. Heyd, E. N. Brothers, K. N. Kudin, V. N. Staroverov, T. A. Keith, R. Kobayashi, J. Normand, K. Raghavachari, A. P. Rendell, J. C. Burant, S. S. Iyengar, J. Tomasi, M. Cossi, J. M. Millam, M. Klene, C. Adamo, R. Cammi, J. W. Ochterski, R. L. Martin, K. Morokuma, O. Farkas, J. B. Foresman and D. J. Fox, Gaussian 16, Revision C.01, Gaussian, Inc.

Acknowledgements

R.V. wishes to thank the Zagreb University Computing Centre (SRCE) for granting computational resources on the SUPEK cluster.

Author contributions

Ida Boček Pavlinac: Formal analysis, Investigation, Data Curation, Writing—Original Draft, Visualization. Mirna Dragić: Investigation, Data Curation, Visualization. Marina Galić: Formal analysis, Investigation, Data Curation. Ana Čikoš: Formal analysis, Investigation, Data Curation, Writing—Original Draft, Visualization. Marijana Hranjec: Conceptualization, Formal analysis, Investigation, Writing—Original Draft, Visualization, Supervision. Robert Vianello: Conceptualization, Formal analysis, Investigation, Writing—Original Draft, Visualization, Supervision, Funding acquisition.

Funding

This work benefited from the financial support of the Croatian Science Foundation through the Grant No. IP-2020-02-8090.

Declarations

Competing interests

The authors declare that they have no known competing financial interests or personal relationships that could have appeared to influence the work reported in this paper.

Additional information

Supplementary Information The online version contains supplementary material available at https://doi.org/10.1038/s41598-026-69550-y.

Correspondence and requests for materials should be addressed to M.H. or R.V.

Reprints and permissions information is available at www.nature.com/reprints.

Publisher's note Springer Nature remains neutral with regard to jurisdictional claims in published maps and institutional affiliations.

Open Access This article is licensed under a Creative Commons Attribution 4.0 International License, which permits use, sharing, adaptation, distribution and reproduction in any medium or format, as long as you give appropriate credit to the original author(s) and the source, provide a link to the Creative Commons licence, and indicate if changes were made. The images or other third party material in this article are included in the article's Creative Commons licence, unless indicated otherwise in a credit line to the material. If material is not included in the article's Creative Commons licence and your intended use is not permitted by statutory regulation or exceeds the permitted use, you will need to obtain permission directly from the copyright holder. To view a copy of this licence, visit http://creativecommons.org/licenses/by/4.0/.

© The Author(s) 2026